Optoacoustic imaging in endocrinology and metabolism

Angelos Karlas[1,2,3], Miguel A. Pleitez[1,2], Juan Aguirre[1,2] and Vasilis Ntziachristos[1,2†]

[1] Center for Translational Cancer Research (TranslaTUM), Technical University of Munich, Germany

[2] Institute of Biological and Medical Imaging, Helmholtz Zentrum München, Neuherberg, Germany

[3] Clinic of Vascular and Endovascular Surgery, Klinikum rechts der Isar, Munich, Germany

[†]E-mail: v.ntziachristos@tum.de; v.ntziachristos@helmholtz-muenchen.de.

Abstract

Imaging is an essential tool in research, diagnostics and the management of endocrine disorders. Ultrasonography, nuclear medicine techniques, MRI, CT and optical methods are already used for applications in endocrinology. Optoacoustic imaging, also termed photoacoustic imaging, is emerging as a method to visualize endocrine physiology and disease at different scales of detail: microscopic, mesoscopic and macroscopic. Optoacoustic contrast arises from endogenous light absorbers, such as oxygenated and deoxygenated haemoglobin, lipids and water, or exogenous contrast agents, and reveals tissue vasculature, perfusion, oxygenation, metabolic activity and inflammation. The development of high-performance optoacoustic scanners for human use has given rise to a variety of clinical investigations, which complement the use of the technology in preclinical research. Here, we review key progress with optoacoustic imaging technology as it relates to applications in endocrinology, for example, to visualise thyroid morphology and function, the microvasculature in diabetes mellitus or adipose tissue metabolism, with particular focus on multispectral optoacoustic tomography and raster-scan optoacoustic mesoscopy. We explain the merits of optoacoustic microscopy and focus on mid-infrared optoacoustic microscopy, which enables label-free imaging of metabolites in cells and tissues. We showcase current optoacoustic applications within endocrinology and discuss the potential of these technologies to advance research and clinical practice.

[H1] Introduction

Imaging has a critical role in the morphological and functional visualization of organs and tissues *in vivo* and is widely used to assess various endocrine disorders in the pituitary, thyroid, adrenal or reproductive

glands, the pancreas, bone and different forms of endocrine tumour[1]. Many of the imaging modalities that are in use can exploit intrinsic tissue contrast; however, techniques also commonly utilize contrast agents to reveal morphological, physiological and biochemical features[2]. Generally, ultrasonography, X-ray computed tomography (CT) and magnetic resonance imaging (MRI) are used for anatomical and physiological imaging of glands or lesions using either intrinsic contrast or contrast agents. In addition, positron emission tomography (PET) and single-photon emission computed tomography (SPECT) imaging extend visualization at the functional and molecular level of the disease, measuring biochemical and metabolic parameters using externally administered radionuclide-based agents (**Table 1**). Despite this wealth of imaging options, a need still exists for portable, low cost and easily disseminated methods that can be safely applied to large populations to assess endocrine and metabolic diseases, which are highly prevalent[3].

Optical imaging in the visible (380–750 nm) or near-infrared (NIR; 750–2500 nm) wavelengths has been considered as an alternative modality to traditional imaging methods (CT or MRI) for endocrinology applications. For example, fluorescence imaging using the fluorescent dye indocyanine green, or parathyroid autofluorescence have been used in endocrine surgery. Specifically, adrenalectomy or thyroidectomy operations have been performed under fluorescence guidance that in the latter scenario improves the detection of the parathyroid glands, which are difficult to identify and are often unnecessarily excised along with the thyroid[4]. In particular, label-free auto-fluorescence imaging showed good potential for detecting parathyroid tissue during surgery[5]. Nevertheless, this method has limited penetration depth (~3 mm) and does not provide information about parathyroid tissue perfusion and oxygenation, which are crucial factors for their preservation during surgery[5].

Hyperspectral imaging (HSI) is a method that collects images of tissue at multiple wavelengths. This technique has also been used intraoperatively to discriminate between thyroid and parathyroid tissues based on spectral changes, which are exhibited due to differences in the concentration of haemoglobin and oxygenation, as well as water and lipid content[6]. Like conventional photography, HSI achieves good spatial resolution (25 μm per pixel[7]) but its penetration depth is shallower than that of fluorescence imaging. Consequently, HSI can only be used to assess the very superficial layers of tissue, which compromises its overall accuracy and diagnostic potential in tissue applications [7,8].

Optical visualization deeper in tissue has been achieved by diffuse optical tomography (DOT), which is a technique that records diffusive light (typically in the NIR range) that has propagated through tissue to a depth of several millimetres to centimetres. Being a tomographic technique, DOT uses mathematical inversion to compute maps of photon absorption and photon scattering in tissue, which are

representative images of haemoglobin concentration and cellular density, respectively. DOT has been explored for non-invasive endocrine imaging of the thyroid gland in computational experiments[9]. Nevertheless, the strong photon scattering by tissue degrades spatial resolution as a function of depth (especially for depths more than 5 mm) and increases uncertainty about the recorded information, especially in terms of quantifying the absorption and scattering contrast. Due to these limitations, DOT and related optical techniques have yet to find wide acceptance in clinical endocrinology.

Optoacoustic imaging is an alternative optical imaging modality that combines the advantages of optical contrast with the ability to provide high-resolution images deep inside tissue. However, while other optical techniques are sensitive to both optical absorption and scattering, contrast in optoacoustic imaging is primarily due to optical absorption only. In this modality, optical contrast is sensed by detecting ultrasound waves, which are excited within tissue, due to the absorption of light of varying intensity by molecules that absorb the light energy (described in more detail later) Without the use of labels, optoacoustic imaging can resolve oxygenated haemoglobin and deoxygenated haemoglobin, melanin, lipids, collagen and water, on the basis of their absorption spectra, by recording optoacoustic images at multiple wavelengths and using spectral unmixing techniques. The technique has been considered since the late 1970s in imaging applications[10,11]. Furthermore, considerable progress was achieved in the following decades that enabled the imaging of tissues *in vivo* in animal models and in humans, resolving contrast from tissue vascularization and oxygenation[12-16]. Nevertheless, it is only in the past 5 years that the technology has sufficiently matured to enable high-performance biomedical imaging in humans outside of dedicated laboratory settings[17-20].

A hand-held implementation of optoacoustics, termed multi-spectral optoacoustic tomography **[G]** (MSOT)**,** has been now uniquely used to assess a number of different conditions associated with endocrinology, in mice and humans, including oxidative metabolism[21,22], muscle oxygenation and hypoxia[23-25], cardiovascular imaging[26-29], muscular dystrophy[18], inflammation[17] or vascularization and total blood volume[30-32]. Importantly, visualization of these conditions is done without the use of contrast agents (label-free), often capitalizing on the use of two or more wavelengths to generate contrast based on the spectrum of intrinsic tissue light absorbing molecules (discussed in detail later). Techniques such as raster-scan optoacoustic mesoscopy **[G]** (RSOM) achieve superior image resolution but at a more superficial tissue depth[33]. By contrast, a 2019 study showed that optoacoustic microscopy extending to the mid-infrared spectral range (2,500–12,000 nm) could achieve unique visualization of proteins, carbohydrates and lipids in label-free mode[34]. More generally, optoacoustic imaging techniques, also referred to using the term 'photoacoustic,' (for example, spectral photoacoustic tomography (sPAT) and photoacoustic

microscopy (PAT))[35-37] have been also applied to humans for imaging breast cancer [20,38] and arthritis[39], or for enabling measurements of animal models[36,40,41].

In this Review, we explore the current status and clinical potential of stand-alone MSOT, RSOM and hybrid optoacoustic and ultrasound systems (OPUS). We explain the principle of operation of optoacoustic imaging and compare it with earlier investigations using optical imaging techniques. We elucidate the biomedical and clinically relevant information that is measured by the technique and focus in particular on label-free interrogations, that is, the types of imaging and contrast that can be achieved without the use of contrast agents. Finally, we describe current applications in endocrinology and discuss the clinical potential of the technology as a portable and safe method that offers high dissemination potential.

[H1] Principles of operation and contrast

Optoacoustic imaging is an optical imaging technique that illuminates tissue with transient light energy, commonly photon pulses in the nanosecond range[36]. Absorption of the excitation light by different molecules in tissue leads to the generation of fast thermo-elastic expansions of the tissue at the site of absorption[42], giving rise to propagating ultrasound waves that can be detected with ultrasound detectors. The ultrasound waves are recorded in multiple positions on the tissue surface. For each detector position and photon pulse, a time-dependent ultrasound signal is recorded, with later times corresponding to optical contrast deeper in tissue and earlier signal times corresponding to shallower tissue. Subsequently, images of absorption are formed by mathematically combining all time signals recorded in all positions using image reconstruction techniques (tomography)[12,33,43]. Optoacoustic imaging is fundamentally a three-dimensional imaging method, as ultrasound detectors can be placed around or scanned across tissue surfaces, thereby enabling imaging along two dimensions, while the depth (or the distance to detector, the third dimension) is retrieved from the time-dependent information contained in propagating ultrasound waves.

The detection of optical absorption using ultrasound detectors rather than optical cameras allows imaging with both high acoustic resolution and high optical contrast, as image formation is governed by the diffraction of generated ultrasound waves and not by the diffusion of light, as for example in DOT [44]. As an ultrasound detector is used for recording ultrasound signals, many optoacoustic implementations also use electronics that utilize the same ultrasound element for the generation of ultrasound waves, therefore also detecting ultrasound images in parallel to the optoacoustic images[28]. As light propagates

in tissue much faster than sound, it is possible to send a light pulse and a sound pulse with a small-time delay (in the micro-second range) to each other and almost simultaneously record both ultrasound and optoacoustic waves for hybrid imaging.

[H2] Spectrum: The fourth dimension. Although images can be formed at a single wavelength, the illumination of tissue at several wavelengths (such as in MSOT) enables the detection of multiple images that provide a fourth dimension, that of spectrum[12]. For example, a typical illumination pattern can scan a spectral range of 700–1,000 nm using 20 different wavelengths with a scan step of 15 nm. In this case, scans of each wavelength produce a stack of 20 images, that is, a 'multispectral stack'. The multispectral stack can be spectrally unmixed to quantify the concentration of different chromophores **[G]** in each pixel of the reconstructed images. This spectral unmixing step uses the recorded MSOT data, as well as a library of known absorption spectra for specific chromophores that are relevant to each application, to produce a set of images that quantitatively map the distribution of the chromophores within the captured field of view (**Figure 1**). Of note, a particular challenge in three-dimensional MSOT spectral unmixing (that is, across different tissue dimensions) is that the interaction between illumination light and tissue depends non-linearly on depth and wavelength. This dependence produces a unique computational problem, which can compromise the quantification, the sensitivity and the specificity of spectral unmixing if not addressed. To overcome this issue, advanced non-linear spectral unmixing techniques have been proposed that provide improved accuracy for the identification of different chromophores in tissue as a function of depth[23,45].

[H2] Optoacoustic contrast and relation to endocrinology applications. Most optoacoustic clinical studies have focused on imaging intrinsic contrast in the NIR, that is, endogenous tissue chromophores (**Table 2**). The NIR is preferred as light can propagate for several centimetres in this spectral region. In particular, imaging oxygenated haemoglobin and deoxygenated haemoglobin in the 650–850 nm spectral window reveals information on tissue physiology that is associated with oxygenation and blood concentration[17,18,21,30]. The summation of oxygenated haemoglobin to deoxygenated haemoglobin relates to total blood volume, a parameter that is associated with inflammation[17,46], whereby the rate of total blood volume following tissue activating stimulation (for example, cold exposure for brown adipose tissue) is indicative of perfusion[21]. In addition, maps of tissue oxygen saturation (SO_2) can be computed as the ratio of oxygenated haemoglobin to total blood volume and the rate of SO_2 relates to oxygen

utilization, that is, oxidative metabolism[17,23,24]. These parameters are relevant for various endocrine conditions, including thyroiditis, perfusion of thyroid nodules or parenchyma, hypoxia, vascularity and metabolic changes in tumours, as reviewed in the next section. Moreover, lipids can be sensed at 930 nm, where they exhibit an absorption peak[29,47] and these measurements can reveal parameters associated with white adipose tissue, brown adipose tissue, as well as the concentration of lipids in the blood stream and specific tissue compartments. Such measurements relate to a number of pathologies associated with lipid disturbances, such as hyperthyroidism, obesity, polycystic ovary syndrome and thyroid or adrenal tumours. Finally, within the NIR region, water can be sensed at the 970 nm absorption peak[29]. Water measurements can be useful as a reference measurement or in evaluating cystic structures in endocrine organs. Of note, studies have shown that it is possible to record collagen at the spectral peak of ~1,000 nm. This information could be useful in imaging patients with osteogenesis imperfecta, a genetic connective tissue disorder that affects several organs and tissues, such as the bones, skin, muscle and teeth[48,49].

Optoacoustic contrast can be enhanced with contrast agents, such as injected dyes, nanoparticles, or in animal models by the expression of a reporter gene[50,51]. Despite the large variety of agents examined in preclinical applications, only a few qualify today for clinical use. For example, indocyanine green is an organic dye that has been widely used for several clinical applications, including retinal angiography and hepatic clearance studies; notably, indocyanine green exhibits a high absorption cross-section in the NIR that is possible to detect with optoacoustics[52]. Gold nanoparticles have also been considered to improve optoacoustic image contrast due to their ability to impart high contrast[53]. Finally, a new class of non-metal nanoparticle formulations is emerging that showcases better photo-stability and even higher absorption cross-sections (and thus improved contrast) than gold particles[52,54]. Nevertheless, the use of external contrast agents in humans requires rigorous safety evaluations and increases the cost and risk of an examination. Therefore, optoacoustic contrast agents are primarily used in animal studies[50,51].

[H1] Optoacoustic imaging implementations

Modern optoacoustic systems have been used for preclinical or clinical applications with a variety of configurations and technical specifications. In optoacoustic imaging, depth and resolution are inversely associated with the ultrasound detector frequency being used[12,55]. For example, by selective imaging at frequencies of a few MHz (for example, central frequency of 4–6 MHz, bandwidth of 0.1–10 MHz), depths

of 2–4 cm can be achieved with a resolution of 200–300 µm (that is, macroscopy). By contrast, imaging at frequencies in the tens of MHz (for example, central frequency of 50 MHz, bandwidth of 10–100 MHz) enables imaging at depths of up to ~1 cm but with resolutions of a few tens of microns (that is, mesoscopy and microscopy) in a scalable fashion (**Figure 1**). Of note, when ultrashort light pulses are used for excitation, all ultrasound frequencies in the tissue are excited. Finally, the use of detectors that capture frequencies at hundreds of MHz (>100 MHz) approach resolutions that are typical of optical microscopy (<10 µm) at depths in the range of a few millimetres (1–2 mm). Alternatively, focused illumination can be used for optoacoustic microscopy, in direct analogy to optical microscopy. In this case, the tissue penetration is also typically sub-millimetre (<1 mm) but with resolutions that obey the laws of optical diffraction, with sub-micrometre lateral resolutions (<1 µm) being possible.

[H2] Macroscopy. The development of fast-tunable, high-energy-per-pulse lasers[12,56] enabled real-time optoacoustic imaging at up to 100 frames per second, with each frame potentially being imaged at a different wavelength. Therefore, these lasers are appropriate for video rate multi-wavelength imaging that could reach 5–10 MSOT frames per second. Detection is based on multi-element ultrasound arrays that detect frequencies in the 3–10 MHz range and corresponding analogue to digital converter arrays, which collect, digitize and store ultrasound signals in parallel and in real-time. For clinical applications (**Figure 2, Figure 3**), hand-held scanners (**Figure 1, Figure 2A**) are typically implemented in hybrid form with ultrasonography, utilizing the same common ultrasound detector array for the emission of ultrasound and detection of ultrasound and optoacoustic signals[21,29]. The same MSOT imaging principle also applies to the imaging of small animals (**Figure 4, Figure 5**). Animal imaging is performed either by hand-held systems or by systems with dedicated small animal imaging holders (**Figure 4A**)[21,57]. For the latter, the anesthetized animal or a tissue sample of interest is typically placed in a cylindrical holder made of a transparent membrane. The membrane is surrounded by water to couple ultrasound to the transducer (another name for the device that records ultrasound). Although scanners for clinical applications cover angles of 100–180 degrees, dedicated animal scanners can reach up to 270 degrees for animals placed horizontally[58] or 360 degrees for animals placed vertically into the imaging chamber[59]. Overall, higher angle coverage provides a more complete data set and leads to improved imaging performance over smaller angle coverage.

[H2] Mesoscopy. Mesoscopy indicates higher resolution imaging (5–100 µm) but requires transducers that can collect higher frequencies and higher bandwidths than macroscopy (that is, they operate in the several tens of MHz and higher, 10-100 MHz). Such high-frequency performance is not commonly achieved by detector arrays, which are generally limited to a few tens of MHz (20–30 MHz)[60]. Therefore, high-performance mesoscopy is typically achieved with broad-band single element detectors, which can operate at a much higher frequency. Due to the use of a single element, mesoscopic imaging requires that the detector is scanned over the tissue, the implementation of which is termed raster-scan optoacoustic mesoscopy (RSOM)[46,61] (**Figure 2C**). Mesoscopy systems operating with detector arrays in the ~20 MHz range have also been reported[62].

The introduction of ultra-wideband (UWB) frequency detection, which reaches more than 200 MHz bandwidth, merges mesoscopic and microscopic resolutions in a single detector setup[33,63,64]. UWB-RSOM has been used to assess the microvasculature in various organs in animals and humans, including human skin, and enables imaging of capillaries close to the epidermis (<10 µm resolution) together with larger arterioles and venules of the deep vascular plexus[60,65]. Typically, the field-of-view of UWB-RSOM spans tens of cubic mm and images can be acquired in a few tens of seconds (15–45 seconds)[66]. Similar to MSOT, illumination at multiple wavelengths with RSOM allows visualization of oxygenated haemoglobin and deoxygenated haemoglobin (**Table 2**), which have been used to resolve microvasculature density, the distribution of oxygenated haemoglobin and deoxygenated haemoglobin, and oxygen saturation in tissue and microvessels[67]. Moreover, measurements of vessel size distribution and vessel density have been used to quantify skin inflammation[68]. Likewise, the imaging of lipids and water has been demonstrated with UWB-RSOM and used to visualize tissue adipose tissue layers and the sebaceous glands[67]. Functional studies can be also performed by means of recording the endothelial-dependent hyperaemic response to a challenge, for example the application of a transient (for example, 3–5 min) cuff occlusion or heat[69-71]. Due to the high resolution and contrast achieved by UWB-RSOM, functional responses of the entire microvascular tree can be recorded in a label-free fashion[69].

[H2] Microscopy. Like RSOM, optoacoustic microscopy also requires raster scanning, either of a high-frequency detector or a focused light beam [61]. Currently, optoacoustic microscopy lacks well-established labels for tagging cell function in comparison with optical microscopy, where fluorescence approaches are more refined. Although the use of tyrosinase **[G]** [72] or other reporters and labels [73,74] has been researched, they have not shown the ubiquitous applicability of fluorescence proteins or agents in optical microscopy. For this reason, a driving force behind the development of optoacoustic operations are their integration

with conventional optical setups, whereby optical performance is complemented by absorption contrast information that originates from optoacoustic detection. A promising demonstration of this premise is the use of optoacoustic microscopy at an extended spectral range in the infrared region. In particular, mid-infrared optoacoustic microscopy **[G]** (MiROM) has been used in the spectral range of 2,500–12,000 nm[34,75] and has enabled the visualization of vibrational transitions of biomolecules, without the need of external labels[34]. MiROM can image proteins, carbohydrates and lipids within living cells, with sensitivity that is superior to that of Raman microscopy[76], which is an optical method that detects inherently weak inelastic scattering of photons.

[H1] Applications in endocrinology

Optoacoustic methods bring a unique label-free ability to record physiological tissue alterations caused by disease, which can be used for basic discovery, advancing diagnostics and monitoring disease progression and therapeutic efficacy. By being portable and using safe light energy, optoacoustic modalities are also appropriate for frequent and longitudinal measurements, and are compatible with the concurrent application of ultrasonography. The use of optoacoustic contrast agents in animal and cell research enables a large profile of biomarkers to be examined. These include features such as angiogenesis and vascular morphology, tissue oxygenation or hypoxia and metabolism[21], inflammation[17,30], lipids and water[29].

[H2] Thyroid disease. The thyroid gland is a highly vascularized organ that produces hormones, which affect organ function, metabolic rate and protein synthesis. Functional imaging of the thyroid offers diagnostics and theranostics (the combination of imaging and treatment delivery in a single system) in structural pathologies (that is, nodules and cancer) or functional pathologies (that is, hyperthyroidism or Graves disease, and Hashimoto thyroiditis or hypothyroidism)[77]. Current imaging techniques can either monitor the uptake of radioactive contrast agents using nuclear medicine techniques or can assess blood flow in the thyroid by Doppler ultrasound.

MSOT could be used for enhanced functional characterization of the thyroid by imaging vascularization and oxygenation based on haemoglobin contrast, whereas imaging of lipid and water content can inform on thyroid pathophysiology parameters. Importantly, initial studies in healthy

volunteers[78] demonstrated the potential of MSOT to visualize vascular features of the thyroid gland. These studies have stimulated interest in optoacoustic imaging of thyroid anatomy (**Figure 2B**) and function in diffuse thyroid diseases or nodular lesions, as well as the possibility of visualizing changes associated with malignancy without labels. In particular, MSOT revealed an increase in total blood volume and a reduction in lipid content within the thyroid parenchyma in patients with Graves disease (*n* = 6) compared with control individuals (*n* = 8)[79] (**Figure 2Bc, Figure 2Bd**). Furthermore, MSOT imaging showed the presence of hypoxia and reduced lipid content in patients with malignant thyroid nodules (*n* = 3) compared with people with benign thyroid nodules (*n* = 13)[79] (**Figure 2Be, Figure 2Bf**). Furthermore, based on haemoglobin contrast, optoacoustic imaging could reveal small vessels in human thyroid cancers not visible by means of Doppler ultrasound, and provided functional parameters beyond the flow visualization that is provided by Doppler readouts[80]. These pilot studies showed the potential of MSOT to provide thyroid gland functional imaging without ionizing radiation or the injection of contrast agents. The short examination times (~5 min) and the portability of MSOT offer convenient use and could enable clinical dissemination.

[H2] Diabetes mellitus, obesity and metabolism. Diabetes mellitus is the most prevalent endocrine disease. Imaging in diabetes mellitus is important for visualizing the functional impairment of pancreatic β-cells and the effects of the disease on the cardiovascular, nervous, gastrointestinal, musculoskeletal and other systems[81,82]. Optoacoustic imaging could be used in patients to stage the severity of diabetes mellitus, by quantitative imaging of diabetic complications. For example, MSOT has been used to image the peripheral vasculature in healthy volunteers, as well as to assess endothelial macrovascular function in the radial artery[32], an early biomarker of atherosclerosis, which is accelerated in diabetes mellitus. Furthermore, based on haemoglobin contrast, MSOT showed promise in imaging the intestines in mice[83] and humans[17], as well as the haemodynamics and oxygenation of peripheral muscle in healthy volunteers[24] and patients with peripheral arterial disease[25], two organs that might be affected in patients with diabetes mellitus and manifest as diabetic enteropathy[84] or myopathy[85], respectively. Skin microvascular structure and reactivity can also be assessed by RSOM in great detail (**Figure 2C**), which has been used in patients to characterize chronic inflammatory diseases, such as psoriasis[46]. These studies showcase RSOM as a highly potent method for imaging skin micro-angiopathy, which is a quantitative indicator of diabetes mellitus[86-89]. Such microvascular impairments might appear before the development of clinically apparent symptoms associated with systemic manifestations of the disease[86]. Therefore, by

using skin microvasculature as a biomarker of diabetes mellitus, RSOM could provide the means for portable characterization and precise staging of diabetic complications.

In addition to haemoglobin contrast, MSOT can visualize lipids and adipose tissue (**Figure 3A**) for assessing endocrine and metabolic functions. The method has been shown to resolve label-free white adipose tissue (WAT) and brown adipose tissue (BAT) depots based on differences in the spectral profiles of the two tissue types[21]. Moreover, cold-induced BAT metabolic activation in volunteers was resolved (**Figure 3B**) using optoacoustic imaging based on SO_2 rate contrast (**Table 1**). The ability to record metabolism using label-free optoacoustics was further supported by mouse studies of BAT activation via norepinephrine injection (described later). Based on the same principle of vasometabolic coupling, whereby metabolic demand dictates blood flow and oxygen consumption, MSOT has been used in healthy volunteers to image muscle perfusion and oxygenation changes as a function of different challenges, such as exercise or blood supply occlusion[24,90]. In a 2019 study, RSOM was used to produce detailed images of intracutaneous lipids in humans along with several other endogenous chromophores (for example, haemoglobin, melanin and water)[67]. Dermal adipose tissue is also implicated in various conditions, including obesity and diabetes mellitus-related pathophysiology[91,92,93], and could be non-invasively investigated using optoacoustic techniques.

[H2] Surgical guidance in endocrine tumours. Optoacoustic imaging has been explored for surgical guidance, in particular for better localizing the tumour mass or to avoid damage to sub-surface vascular structures. This potential has been explored in various surgeries, including ovarian cancer[94] or pancreatic cancer[95], as well as in endocrine tumour surgery, that is, trans-sphenoidal surgical removal of pituitary tumours[96]. Furthermore, the use of optoacoustic guidance has been suggested for avoiding carotid artery trauma during surgical procedures of the pituitary, using a miniaturized optoacoustic warning device based on an optical fibre mounted on the surgical tool[97].

[H2] Research applications and animal studies. Optoacoustic imaging has been used as a research tool in many animal studies and can offer high-resolution whole-body mouse imaging. For example, protease activity was investigated in FTC133 thyroid tumours implanted in the hind legs of mice[98], using imaging agents sensitive to matrix metalloproteinases MMP-2 and MMP-9 resolved by small-animal MSOT. Optoacoustic imaging has been also used to characterize bone microstructure in an animal model of postmenopausal osteoporosis[99]. This study was conducted on excised femur bone specimens of female

rats that underwent ovariectomy, or underwent ovariectomy and received intraperitoneal bone preservation therapy with zoledronic acid, or sham-operated controls. The bone samples were examined by analysing the frequency spectra of the measured optoacoustic signals. Activation of BAT in mice was also possible based on recording the SO_2 rate (**Table 2**) after activation by norepinephrine[21], secretin[57] or icilin[100], which all induce BAT thermogenesis. In these studies, MSOT readouts showed a clear increase in both oxygenated haemoglobin and deoxygenated haemoglobin signals in activated BAT compared with BAT in the resting state (**Figure 4B**). An increase in total blood volume within the interscapular BAT region after BAT activation was also recorded in these studies.

In addition to small animal research, the development of mid-infrared optoacoustic microscopy (MiROM)[34] has demonstrated label-free imaging of metabolic parameters, such as lipids, carbohydrates and proteins in living cells (**Figure 5**). For example, MiROM was used to visualize the spatiotemporal dynamics of lipid droplets during isoproterenol-induced lipolysis in brown adipocytes (derived from differentiated precursor BAT) and white adipocytes (differentiated 3T3-L1). Due to its ability to visualize bond-specific molecular contrast, MiROM might enable the direct monitoring of hormones during metabolic processes. For instance, amino acid-based or protein-based hormones (such as insulin) could be detected using the amide I and amide II absorption bands, whereas steroids (for example, cortisol) could be detected by their absorption bands in the fingerprint region[101]. MiROM could be further combined with imaging in other spectral regions, such as the visible (380–750 nm), to observe tissue vascularization and oxygenation[102], or the NIR (780–2,500 nm) to monitor lipid metabolism[103]. Furthermore, MIROM can be easily combined with other microscopy techniques in multimodal hybrid setups[104] to reveal interesting crosstalk among several biological pathways[105-107].

[H1] Conclusions

Optoacoustic imaging offers four major strengths that drive its consideration in endocrinology studies. First, it solves the fundamental limitations of optical imaging, enabling for the first time high-resolution and quantitative imaging of chromophores deep in tissues *in vivo*. Second, it provides non-invasive, label-free imaging of contrasts that relate to tissue function and metabolism. Third, it can operate concurrently with ultrasonography, using the same ultrasound detector, enabling the simultaneous collection of complementary information. Finally, it offers portability and safe technology that can be used for frequent and longitudinal studies.

The abovementioned strengths of optoacoustic imaging come with limitations that could affect its usefulness for endocrinology. Despite reaching unprecedented depths at high resolution for a light-based imaging technique (for example, 2–4 cm for MSOT), optoacoustic imaging still offers poor penetration depths compared with other techniques (for example, PET, MRI or X-Ray; **Table 1**) due to the attenuation of light energy with depth. Thus, imaging deeper organs (for example, pancreas or adrenal glands) or adipose tissue with optoacoustic techniques is a challenge. Furthermore, many current optoacoustic systems are hand-held, which necessitates a trade-off between practicality and accuracy. Hand-held probes are equipped with small ultrasound detector arrays in geometries that cover limited viewing angles (for example, 130-180°). The limited viewing angles introduce inaccuracies into the final representation of the true sizes of the anatomical structures and hinder precise interpretation of data. The design of novel optoacoustic image reconstruction algorithms that compensate for the abovementioned artefacts is expected to further improve the accuracy of recorded images. Moreover, optoacoustic imaging, especially clinical technologies (for example, MSOT and RSOM), are vulnerable to motion artefacts that degrade image quality. These artefacts might be patient-dependent (such as pulsation, breathing or voluntary patient motion) or operator-dependent (for example, irregular movements of the probe during scanning). Several algorithms have been developed to provide motion correction for microscopic, mesoscopic (for example, RSOM) and macroscopic (for example, MSOT) optoacoustic applications [108-110].

As different applications develop in endocrinology, we expect a disseminated use of the technology in studying metabolic and functional conditions associated with the progression of various diseases. Thus, optoacoustics could facilitate promising avenues of future research in the field of endocrinology, such as the investigation of adipose tissues in obesity and during obesity treatments, neuroendocrine tumours, diabetic microangiopathy and cellular lipid dynamics in cardiometabolic diseases, heading towards a more precise assessment of disease staging and the effects of possible interventions.

1 Chrousos, G. P. Organization and Integration of the Endocrine System. *Sleep Med Clin* **2**, 125-145 (2007).

2 Shaw, A. S. & Cheow, H. K. Imaging in endocrinology. *Medicine* **45**, 456-463 (2017).

3 Golden, S. H., Robinson, K. A., Saldanha, I., Anton, B. & Ladenson, P. W. Clinical review: Prevalence and incidence of endocrine and metabolic disorders in the United States: a comprehensive review. *J Clin Endocrinol Metab* **94**, 1853-1878 (2009).

4 Kahramangil, B. & Berber, E. The use of near-infrared fluorescence imaging in endocrine surgical procedures. *J Surg Oncol* **115**, 848-855 (2017).

5 Liu, J. *et al.* Near-infrared auto-fluorescence spectroscopy combining with Fisher's linear discriminant analysis improves intraoperative real-time identification of normal parathyroid in thyroidectomy. *BMC Surg* **20**, 4 (2020).
6 Barberio, M. *et al.* Hyperspectral based discrimination of thyroid and parathyroid during surgery. *Current Directions in Biomedical Engineering* **4**, 399-402 (2018).
7 Halicek, M., Fabelo, H., Ortega, S., Callico, G. M. & Fei, B. in *Cancers (Basel)* Vol. 11 (2019).
8 Kho, E. *et al.* Imaging depth variations in hyperspectral imaging: Development of a method to detect tumor up to the required tumor-free margin width. *J Biophotonics* **12**, e201900086 (2019).
9 Fujii, H., Yamada, Y., Kobayashi, K., Watanabe, M. & Hoshi, Y. Modeling of light propagation in the human neck for diagnoses of thyroid cancers by diffuse optical tomography. *Int J Numer Method Biomed Eng* https://doi.org/10.1002/cnm.2826 (2017).
10 Busse, G. & Rosencwaig, A. Subsurface imaging with photoacoustics. *Applied Physics Letters* **36**, 815-816 (1980).
11 Rosencwaig, A. Potential clinical applications of photoacoustics. *Clin Chem* **28**, 1878-1881 (1982).
12 Taruttis, A. & Ntziachristos, V. Advances in real-time multispectral optoacoustic imaging and its applications. *Nature Photonics* **9**, 219-227 (2015).
This paper provides a comprehensive overview of the MSOT technology and its applications.

13 Oraevsky, A., Jacques, S., Esenaliev, R. & Tittel, F. *Laser-based optoacoustic imaging in biological tissues*. Vol. 2134 PWL (SPIE, 1994).
14 Oraevsky, A. A. *et al.* in *BiOS '99 International Biomedical Optics Symposium* Vol. 3597 352-364 (International Society for Optics and Photonics, 1999).
15 Esenaliev, R. O. *et al.* Optoacoustic technique for noninvasive monitoring of blood oxygenation: a feasibility study. *Applied optics* **41**, 4722-4731 (2002).
16 Esenaliev, R. O., Petrov, Y. Y., Hartrumpf, O., Deyo, D. J. & Prough, D. S. Continuous, noninvasive monitoring of total hemoglobin concentration by an optoacoustic technique. *Applied optics* **43**, 3401-3407 (2004).
17 Knieling, F. *et al.* Multispectral Optoacoustic Tomography for Assessment of Crohn's Disease Activity. *N Engl J Med* **376**, 1292-1294 (2017).
An original research paper on MSOT imaging of inflammatory bowel disease.

18 Regensburger, A. P. *et al.* Detection of collagens by multispectral optoacoustic tomography as an imaging biomarker for Duchenne muscular dystrophy. *Nat Med* **25**, 1905-1915 (2019).
An original research paper on MSOT imaging of collagen in Duchene muscular dystrophy.

19 Stoffels, I. *et al.* Metastatic status of sentinel lymph nodes in melanoma determined noninvasively with multispectral optoacoustic imaging. *Science translational medicine* **7**, 317ra199 (2015).
20 Menezes, G. L. G. *et al.* Downgrading of Breast Masses Suspicious for Cancer by Using Optoacoustic Breast Imaging. *Radiology* **288**, 355-365 (2018).
21 Reber, J. *et al.* Non-invasive Measurement of Brown Fat Metabolism Based on Optoacoustic Imaging of Hemoglobin Gradients. *Cell Metabolism* **27**, 689-701 (2018).
An original research paper on MSOT imaging of brown adipose tissue activation based on haemoglobin contrast.

22 Ntziachristos, V., Pleitez, M. A., Aime, S. & Brindle, K. M. Emerging Technologies to Image Tissue Metabolism. *Cell Metab* **29**, 518-538 (2019).

This review provides a comprehensive overview of the novel technologies used in imaging metabolism.

23 Tzoumas, S. *et al.* Eigenspectra optoacoustic tomography achieves quantitative blood oxygenation imaging deep in tissues. *Nature communications* **7**, 12121 (2016).
24 Karlas, A. *et al.* Multispectral Optoacoustic Tomography of Muscle Perfusion and Oxygenation under Arterial and Venous Occlusion - A Human Pilot Study. *J Biophotonics* **13,** e201960169 (2020).
25 Karlas, A. *et al.* Multispectral optoacoustic tomography of peripheral arterial disease based on muscle hemoglobin gradients—a pilot clinical study. *Annals of Translational Medicine* **9,** 36 (2021).
26 Taruttis, A. *et al.* Optoacoustic Imaging of Human Vasculature: Feasibility by Using a Handheld Probe. *Radiology* **281,** 152160 (2016).
27 Masthoff, M. *et al.* Use of Multispectral Optoacoustic Tomography to Diagnose Vascular Malformations. *JAMA dermatology* **154,** 1457-1462 (2018).
28 Yang, H. *et al.* Soft ultrasound priors in optoacoustic reconstruction: Improving clinical vascular imaging. *Photoacoustics* **19**, 100172 (2020).
29 Karlas, A. *et al.* Cardiovascular optoacoustics: From mice to men - A review. *Photoacoustics* **14**, 19-30 (2019).
30 Diot, G. *et al.* Multispectral Optoacoustic Tomography (MSOT) of Human Breast Cancer. *Clinical cancer research : an official journal of the American Association for Cancer Research* **23**, 6912-6922 (2017).

An original research paper on MSOT imaging of human breast cancer.

31 Masthoff, M. *et al.* Use of Multispectral Optoacoustic Tomography to Diagnose Vascular Malformations. *JAMA dermatology* **154**, 1457-1462 (2018).
32 Karlas, A. *et al.* Flow-mediated dilatation test using optoacoustic imaging: a proof-of-concept. *Biomedical Optics Express* **8**, 3395-3403 (2017).
33 Omar, M., Aguirre, J. & Ntziachristos, V. Optoacoustic mesoscopy for biomedicine. *Nature Biomedical Engineering* **3,** 354–370 (2019).

This paper provides a comprehensive overview of the RSOM technology and its biomedical applications.

34 Pleitez, M. A. *et al.* Label-free metabolic imaging by mid-infrared optoacoustic microscopy in living cells. *Nat Biotechnol* **38**, 293–296 (2020).

An original research paper on MiROM technology and its use in imaging of cellular metabolites.

35 Steinberg, I. *et al.* Photoacoustic clinical imaging. *Photoacoustics* **14**, 77-98 (2019).
36 Beard, P. Biomedical photoacoustic imaging. *Interface Focus* **1**, 602-631 (2011).
37 Yao, J. & Wang, L. V. Photoacoustic Microscopy. *Laser Photon Rev* https://doi.org/10.1002/lpor.201200060 (2013).
38 Oraevsky, A. A. *et al.* Clinical optoacoustic imaging combined with ultrasound for coregistered functional and anatomical mapping of breast tumors. *Photoacoustics* **12**, 30-45 (2018).
39 Jo, J. *et al.* A Functional Study of Human Inflammatory Arthritis Using Photoacoustic Imaging. *Scientific reports* **7**, 15026 (2017).
40 Zhang, H. F., Maslov, K., Stoica, G. & Wang, L. V. Functional photoacoustic microscopy for high-resolution and noninvasive in vivo imaging. *Nat Biotechnol* **24**, 848-851 (2006).
41 Cox, B., Laufer, J. G., Arridge, S. R. & Beard, P. C. Quantitative spectroscopic photoacoustic imaging: a review. *J Biomed Opt* **17**, 061202 (2012).

42 Wang, L. V. & Yao, J. A practical guide to photoacoustic tomography in the life sciences. *Nat Methods* **13**, 627-638 (2016).
43 Lutzweiler, C. & Razansky, D. Optoacoustic imaging and tomography: reconstruction approaches and outstanding challenges in image performance and quantification. *Sensors (Basel, Switzerland)* **13**, 7345-7384 (2013).
44 Ntziachristos, V. & Razansky, D. Molecular imaging by means of multispectral optoacoustic tomography (MSOT). *Chemical reviews* **110**, 2783-2794 (2010).
45 Olefir, I., Tzoumas, S., Yang, H. & Ntziachristos, V. A Bayesian Approach to Eigenspectra Optoacoustic Tomography. *IEEE Trans Med Imaging* **37**, 2070-2079 (2018).
46 Aguirre, J. *et al.* Precision assessment of label-free psoriasis biomarkers with ultra-broadband optoacoustic mesoscopy. *Nature Biomedical Engineering* **1**, 0068 (2017).
An original research paper on RSOM technology and its use in imaging of skin inflammation in psoriasis.

47 Shaw, A. & Mantsch, H. Infrared Spectroscopy of Biological Fluids in Clinical and Diagnostic Analysis. *Encyclopedia of Analytical Chemistry* https://doi.org/10.1002/9780470027318.a0106.pub2 (2008).
48 Lindahl, K., Langdahl, B., Ljunggren, O. & Kindmark, A. Treatment of osteogenesis imperfecta in adults. *Eur J Endocrinol* **171**, R79-90 (2014).
49 Veilleux, L. N., Trejo, P. & Rauch, F. in *J Musculoskelet Neuronal Interact* Vol. 17 1-7 (2017).
50 Gujrati, V., Mishra, A. & Ntziachristos, V. Molecular imaging probes for multi-spectral optoacoustic tomography. *Chemical communications (Cambridge, England)* **53**, 4653-4672 (2017).
51 Weber, J., Beard, P. C. & Bohndiek, S. E. Contrast agents for molecular photoacoustic imaging. *Nat Methods* **13**, 639-650 (2016).
52 Beziere, N. *et al.* Dynamic imaging of PEGylated indocyanine green (ICG) liposomes within the tumor microenvironment using multi-spectral optoacoustic tomography (MSOT). *Biomaterials* **37**, 415-424 (2015).
53 Li, W. & Chen, X. Gold nanoparticles for photoacoustic imaging. *Nanomedicine (London, England)* **10**, 299-320 (2015).
54 Gujrati, V. *et al.* Bioengineered bacterial vesicles as biological nano-heaters for optoacoustic imaging. *Nat Commun* **10**, 1114 (2019).
55 Ntziachristos, V. Going deeper than microscopy: the optical imaging frontier in biology. *Nat Methods* **7**, 603-614 (2010).
56 Buehler, A., Kacprowicz, M., Taruttis, A. & Ntziachristos, V. Real-time handheld multispectral optoacoustic imaging. *Opt Lett* **38**, 1404-1406 (2013).
57 Li, Y. *et al.* Secretin-Activated Brown Fat Mediates Prandial Thermogenesis to Induce Satiation. *Cell* **175**, 1561-1574 (2018).
58 Park, S. J. *et al.* Visualizing Alzheimer's Disease Mouse Brain with Multispectral Optoacoustic Tomography using a Fluorescent probe, CDnir7. *Scientific reports* **9**, 12052 (2019).
59 Ermilov, S. *et al. 3D laser optoacoustic ultrasonic imaging system for research in mice (LOUIS-3DM)*. Vol. 8943 PWB (SPIE, 2014).
60 Schwarz, M., Omar, M., Buehler, A., Aguirre, J. & Ntziachristos, V. Implications of ultrasound frequency in optoacoustic mesoscopy of the skin. *IEEE transactions on medical imaging* **34**, 672-677 (2015).
61 Aguirre, J. *et al.* Broadband mesoscopic optoacoustic tomography reveals skin layers. *Opt Lett* **39**, 6297-6300 (2014).

62 Chekkoury, A. *et al.* High-Resolution Multispectral Optoacoustic Tomography of the Vascularization and Constitutive Hypoxemia of Cancerous Tumors. *Neoplasia (New York, N.Y.)* **18**, 459-467 (2016).
63 Omar, M., Soliman, D., Gateau, J. & Ntziachristos, V. Ultrawideband reflection-mode optoacoustic mesoscopy. *Optics letters* **39**, 3911-3914 (2014).
64 Omar, M., Gateau, J. & Ntziachristos, V. Raster-scan optoacoustic mesoscopy in the 25-125 MHz range. *Optics letters* **38**, 2472-2474 (2013).
65 Aguirre, J. *et al.* Broadband mesoscopic optoacoustic tomography reveals skin layers. *Optics letters* **39**, 6297 (2014).
66 Schwarz, M. *et al.* Optoacoustic Dermoscopy of the Human Skin: Tuning Excitation Energy for Optimal Detection Bandwidth With Fast and Deep Imaging in vivo. *IEEE transactions on medical imaging* **36**, 1287-1296 (2017).
67 Berezhnoi, A. *et al.* Optical features of human skin revealed by optoacoustic mesoscopy in the visible and short-wave infrared regions. *Opt Lett* **44**, 4119-4122 (2019).
68 Schwarz, M., Buehler, A., Aguirre, J. & Ntziachristos, V. Three-dimensional multispectral optoacoustic mesoscopy reveals melanin and blood oxygenation in human skin in vivo. *Journal of biophotonics* **9**, 55-60 (2016).
69 Berezhnoi, A. *et al.* Assessing hyperthermia-induced vasodilation in human skin in vivo using optoacoustic mesoscopy. *J Biophotonics* **11**, e201700359 (2018).
70 Subochev, P. *et al.* Raster-scan optoacoustic angiography reveals 3D microcirculatory changes during cuffed occlusion. *Laser Physics Letters* **15**, 045602 (2018).
71 Cracowski, J. L., Minson, C. T., Salvat-Melis, M. & Halliwill, J. R. Methodological issues in the assessment of skin microvascular endothelial function in humans. *Trends in pharmacological sciences* **27**, 503-508 (2006).
72 Jathoul, A. P. *et al.* Deep Deep in vivo photoacoustic imaging of mammalian tissues using a tyrosinase-based genetic reporter. *Nature Photonics* **9**, 239-246 (2015).
73 Krumholz, A., Shcherbakova, D. M., Xia, J., Wang, L. V. & Verkhusha, V. V. Multicontrast photoacoustic in vivo imaging using near-infrared fluorescent proteins. *Scientific reports* **4**, 3939 (2014).
74 Stiel, A. C. *et al.* High-contrast imaging of reversibly switchable fluorescent proteins via temporally unmixed multispectral optoacoustic tomography. *Optics Letters* **40**, 367-370 (2015).
75 Shi, J. *et al.* High-resolution, high-contrast mid-infrared imaging of fresh biological samples with ultraviolet-localized photoacoustic microscopy. *Nat Photonics* **13**, 609-615 (2019).
76 Zhao, Z., Shen, Y., Hu, F. & Min, W. Applications of vibrational tags in biological imaging by Raman microscopy. *Analyst* **142**, 4018-4029 (2017).
77 Walsh, J. P. Managing thyroid disease in general practice. *Med J Aust* **205**, 179-184 (2016).
78 Dima, A. & Ntziachristos, V. In-vivo handheld optoacoustic tomography of the human thyroid. *Photoacoustics* **4**, 65-69 (2016).
79 Roll, W. *et al.* Multispectral optoacoustic tomography of benign and malignant thyroid disorders - a pilot study. *J Nucl Med* **60,** 1461-146 (2019).
80 Yang, M. *et al.* Photoacoustic/ultrasound dual imaging of human thyroid cancers: an initial clinical study. *Biomed Opt Express* **8**, 3449-3457 (2017).
81 Zhang, L. & Thurber, G. Imaging in Diabetes. *In Imaging and Metabolism* (Eds. Lewis J.S. & Keshari K.R.) 175-197 (Springer, Cham, 2018).
82 Rastogi, R. Imaging in Diabetes Mellitus. *Archives of Clinical Nephrology* https://doi.org/10.17352/acn.000009 (2016).
83 Knieling, F. *et al.* Raster-Scanning Optoacoustic Mesoscopy for Gastrointestinal Imaging at High Resolution. *Gastroenterology* **154**, 807-809 (2018).

84 Gotfried, J., Priest, S. & Schey, R. Diabetes and the Small Intestine. *Curr Treat Options Gastroenterol* **15**, 490-507 (2017).
85 Hernández-Ochoa, E. O. & Vanegas, C. Diabetic Myopathy and Mechanisms of Disease. *Biochem Pharmacol (Los Angel)* **4,** 1000e179 (2015).
86 Sörensen, B. M. *et al.* Prediabetes and Type 2 Diabetes Are Associated With Generalized Microvascular Dysfunction. *Circulation* **134**, 1339-1352 (2016).
87 McMillan, D. E. Deterioration of the Microcirculation in Diabetes. *Diabetes* **24**, 944-957 (1975).
88 Levy Bernard, I. *et al.* Impaired Tissue Perfusion. *Circulation* **118**, 968-976 (2008).
89 Fuchs, D., Dupon, P. P., Schaap, L. A. & Draijer, R. The association between diabetes and dermal microvascular dysfunction non-invasively assessed by laser Doppler with local thermal hyperemia: a systematic review with meta-analysis. *Cardiovasc Diabetol* **16,** 11 (2017).
90 Diot, G., Dima, A. & Ntziachristos, V. Multispectral opto-acoustic tomography of exercised muscle oxygenation. *Opt Lett* **40**, 1496-1499 (2015).
91 Guerrero-Juarez, C. F. & Plikus, M. V. Emerging nonmetabolic functions of skin fat. *Nat Rev Endocrinol* **14**, 163-173 (2018).
92 Miranda, J. J., Taype-Rondan, A., Tapia, J. C., Gastanadui-Gonzalez, M. G. & Roman-Carpio, R. Hair Follicle Characteristics as Early Marker of Type 2 Diabetes. *Med Hypotheses* **95**, 39-44 (2016).
93 Baltzis, D., Eleftheriadou, I. & Veves, A. Pathogenesis and treatment of impaired wound healing in diabetes mellitus: new insights. *Adv Ther* **31**, 817-836 (2014).
94 Rindi, G. *et al.* A common classification framework for neuroendocrine neoplasms: an International Agency for Research on Cancer (IARC) and World Health Organization (WHO) expert consensus proposal. *Mod Pathol* **31**, 1770-1786 (2018).
95 Tummers, W. S. *et al.* Intraoperative Pancreatic Cancer Detection using Tumor-Specific Multimodality Molecular Imaging. *Ann Surg Oncol* **25**, 1880-1888 (2018).
96 Lediju Bell, M. A., Ostrowski, A. K., Li, K., Kazanzides, P. & Boctor, E. M. Localization of Transcranial Targets for Photoacoustic-Guided Endonasal Surgeries. *Photoacoustics* **3**, 78-87 (2015).
97 Padhye, V., Valentine, R. & Wormald, P. J. Management of Carotid Artery Injury in Endonasal Surgery. *Int Arch Otorhinolaryngol* **18**, S173-178 (2014).
98 Levi, J. *et al.* Molecular Photoacoustic Imaging of Follicular Thyroid Carcinoma. *Clinical cancer research : an official journal of the American Association for Cancer Research* **19**, 1494-1502 (2013).
99 Feng, T. *et al.* Characterization of bone microstructure using photoacoustic spectrum analysis. *Opt Express* **23**, 25217-25224 (2015).
100 Clemmensen, C. *et al.* Coordinated targeting of cold and nicotinic receptors synergistically improves obesity and type 2 diabetes. *Nat Commun* **9**, 4304 (2018).
101 Lemes, L. C., Caetano Júnior, P. C., Strixino, J. F., Aguiar, J. & Raniero, L. Analysis of serum cortisol levels by Fourier Transform Infrared Spectroscopy for diagnosis of stress in athletes. *Research on Biomedical Engineering* **32**, 293-300 (2016).
102 Rao, B. *et al.* Optical Resolution Photoacoustic Microscopy of Ovary and Fallopian Tube. *Scientific reports* **9**, 14306 (2019).
103 Buma, T., Conley, N. C. & Choi, S. W. Multispectral photoacoustic microscopy of lipids using a pulsed supercontinuum laser. *Biomed Opt Express* **9**, 276-288 (2018).
104 Yakovlev, V. V. *et al.* Stimulated Raman photoacoustic imaging. *Proc Natl Acad Sci U S A* **107**, 20335-20339 (2010).
105 Seeger, M., Karlas, A., Soliman, D., Pelisek, J. & Ntziachristos, V. Multimodal optoacoustic and multiphoton microscopy of human carotid atheroma. *Photoacoustics* **4**, 102-111 (2016).

106 Tserevelakis, G. J., Soliman, D., Omar, M. & Ntziachristos, V. Hybrid multiphoton and optoacoustic microscope. *Opt Lett* **39**, 1819-1822 (2014).
107 Kellnberger, S. *et al.* Optoacoustic microscopy at multiple discrete frequencies. *Light Sci Appl* **7**, 109 (2018).
108 Zhao, H. *et al.* Motion Correction in Optical Resolution Photoacoustic Microscopy. *IEEE Trans Med Imaging* **38**, 2139-2150 (2019).
109 Schwarz, M., Garzorz-Stark, N., Eyerich, K., Aguirre, J. & Ntziachristos, V. Motion correction in optoacoustic mesoscopy. *Scientific reports* **7**, 10386 (2017).
110 Ron, A., Davoudi, N., Deán-Ben, X. L. & Razansky, D. Self-Gated Respiratory Motion Rejection for Optoacoustic Tomography. *Applied Sciences* **9**, 2737 (2019).
111 Trimboli, P. *et al.* Ultrasound and ultrasound-related techniques in endocrine diseases. *Minerva Endocrinol* **43**, 333-340 (2018).
112 Barsanti, C., Lenzarini, F. & Kusmic, C. Diagnostic and prognostic utility of non-invasive imaging in diabetes management. *World J Diabetes* **6**, 792-806 (2015).
113 De Sanctis, V. *et al.* Hand X-ray in pediatric endocrinology: Skeletal age assessment and beyond. *Indian J Endocrinol Metab* **18**, S63-71 (2014).
114 Pisani, P. *et al.* Screening and early diagnosis of osteoporosis through X-ray and ultrasound based techniques. *World J Radiol* **5**, 398-410 (2013).
115 Piciucchi, S., Poletti, V., Sverzellati, N., Gavelli, G. & Carloni, A. Primary and secondary hyperparathyroidism: Findings on chest X-rays and high resolution CT. *European Journal of Radiology Extra* **70**, e107-e110 (2009).
116 Marmin, C. *et al.* Computed tomography of the parathyroids: The value of density measurements to distinguish between parathyroid adenomas of the lymph nodes and the thyroid parenchyma. *Diagnostic and Interventional Imaging* **93,** 597-603 (2012).
117 Wang, F. *et al.* CT and MRI of adrenal gland pathologies. *Quant Imaging Med Surg* **8**, 853-875 (2018).
118 Stein, A. L., Levenick, M. N. & Kletzky, O. A. Computed tomography versus magnetic resonance imaging for the evaluation of suspected pituitary adenomas. *Obstet Gynecol* **73**, 996-999 (1989).
119 Huh, J. *et al.* Optimal Phase of Dynamic Computed Tomography for Reliable Size Measurement of Metastatic Neuroendocrine Tumors of the Liver: Comparison between Pre- and Post-Contrast Phases. *Korean J Radiol* **19**, 1066-1076 (2018).
120 Gausden, E. B., Nwachukwu, B. U., Schreiber, J. J., Lorich, D. G. & Lane, J. M. Opportunistic Use of CT Imaging for Osteoporosis Screening and Bone Density Assessment: A Qualitative Systematic Review. *J Bone Joint Surg Am* **99**, 1580-1590 (2017).
121 Nael, K. *et al.* Dynamic 4D MRI for Characterization of Parathyroid Adenomas: Multiparametric Analysis. *AJNR Am J Neuroradiol* **36**, 2147-2152 (2015).
122 Chang, G. *et al.* MRI Assessment of Bone Structure and Microarchitecture. *Journal of magnetic resonance imaging : JMRI* **46**, 323-337 (2017).
123 Takatsu, Y., Okada, T., Miyati, T. & Koyama, T. Magnetic resonance imaging relaxation times of female reproductive organs. *Acta Radiol* **56**, 997-1001 (2015).
124 Reznek, R. H. CT/MRI of neuroendocrine tumours. *Cancer Imaging* **6**, S163-177 (2006).
125 Davidson, C. Q., Phenix, C. P., Tai, T., Khaper, N. & Lees, S. J. Searching for novel PET radiotracers: imaging cardiac perfusion, metabolism and inflammation. *American journal of nuclear medicine and molecular imaging* **8**, 200-227 (2018).
126 Pacak, K., Eisenhofer, G. & Goldstein, D. S. Functional imaging of endocrine tumors: role of positron emission tomography. *Endocr Rev* **25**, 568-580 (2004).
127 Lu, F. M. & Yuan, Z. PET/SPECT molecular imaging in clinical neuroscience: recent advances in the investigation of CNS diseases. *Quant Imaging Med Surg* **5**, 433-447 (2015).

128 Ichise, M. & Harris, P. E. Imaging of β-Cell Mass and Function. *J Nucl Med* **51**, 1001-1004 (2010).
129 Bernardo-Filho, M., Santos-Filho, S. D., Fonseca, A. d. S. d., Carter, K. & Missailidis, S. Nuclear medicine procedures for the evaluation of male sexual organs: a brief review. *Brazilian Archives of Biology and Technology* **51**, 13-21 (2008).
130 Hopkins, C. R. & Reading, C. C. Thyroid and parathyroid imaging. *Semin Ultrasound CT MR* **16**, 279-295 (1995).
131 Brabander, T., Kwekkeboom, D. J., Feelders, R. A., Brouwers, A. H. & Teunissen, J. J. Nuclear Medicine Imaging of Neuroendocrine Tumors. *Front Horm Res* **44**, 73-87 (2015).
132 Avram, A. M., Fig, L. M. & Gross, M. D. Adrenal gland scintigraphy. *Semin Nucl Med* **36**, 212-227 (2006).
133 Yao, A., Balchandani, P. & Shrivastava, R. K. Metabolic in vivo visualization of pituitary adenomas: a systematic review of imaging modalities. *World Neurosurg* **104**, 489-498 (2017).
134 Karlas, A., Reber, J., Liapis, E., Paul-Yuan, K. & Ntziachristos, V. Multispectral Optoacoustic Tomography of Brown Adipose Tissue. *Handb Exp Pharmacol* **251**, 325-336 (2019).

Acknowledgements

The authors acknowledge the support of funding from European Union's Horizon 2020 research and innovation programme under grant agreement No 871763 (WINTHER) and from the European Research Council (ERC) under grant agreement No 694968 (PREMSOT) and from the Deutsche Forschungsgemeinschaft (DFG), Germany [Gottfried Wilhelm Leibniz Prize 2013; NT 3/10-1].

Author contributions

The authors contributed equally to all aspects of the article.

Peer reviewer information

Nature Reviews Endocrinology thanks the anonymous reviewers for their contribution to the peer review of this work

Competing interests

V.N. has stock and stock options in iThera Medical. All other authors have no conflicts of interest to declare.

Key points

- Optoacoustic technology includes a range of non-invasive, label-free and portable imaging modalities, which provide molecular visualizations at the macroscopic, mesoscopic and microscopic scale.
- Multi-spectral optoacoustic tomography (MSOT) produces real-time tomographic views of tissue with a resolution of 200–300 μm (macroscopy) at depths of 2–4 cm.
- Raster-scan optoacoustic mesoscopy (RSOM) provides volumetric images of tissue microvasculature and perfusion with a resolution of <10 μm (mesoscopy) at depths of 1–2 mm.
- Mid-infrared optoacoustic microscopy (MiROM) provides label-free visualizations of the spatiotemporal dynamics of biomolecules in cellular metabolism.
- Optoacoustic imaging offers a complete framework for investigating anatomic, functional and molecular aspects of common endocrine disorders.

Table 1: Imaging modalities in clinical endocrinology – uses, advantages and disadvantages

Modality	Clinical use in endocrinology	Advantages	Disadvantages
Ultrasonography[111,112]	Imaging thyroid, parathyroid, adrenal or reproductive glands, assessing diabetes mellitus (i.e., imaging pancreas, kidneys, blood vessels, heart and/or adipose tissue), endocrine tumours	Non-ionizing, real-time, fast, portable, easy to use, patient-convenient, high resolution-to-depth ratio, functional information	Low contrast, no direct molecular information, mediocre penetration depth
X-rays [113-115]	Imaging bone (e.g. skeletal age, osteoporosis, hyperparathyroidism)	Fast, convenient for patient and practitioner, portable, high resolution-to-depth ratio	Ionizing radiation, low contrast, no molecular contrast, not real-time, no functional information, limited applications
CT [112,116-120]	Imaging adrenal, pituitary, thyroid, or parathyroid glands, assessing diabetes mellitus (i.e. imaging blood vessels, heart and/or adipose tissue), neuroendocrine tumours, bones	Whole-body imaging, high penetration depth, high resolution-to-depth ratio	Ionizing radiation, no direct molecular information, not real-time, long scanning times, inconvenient for patient, non-portable, requires trained specialist, mediocre contrast, possibly toxic contrast agents
MRI [112,117,118,121-124]	Imaging adrenal, pituitary, thyroid, parathyroid, bone, assessing diabetes mellitus (i.e. imaging pancreas, kidneys, blood vessels, brain, heart and/or adipose tissue), neuroendocrine tumours, reproductive glands	Non-ionizing, whole-body imaging, high resolution-to-depth ratio, high contrast, real-time, functional information, might provide molecular contrast	Long scanning times, not portable, requires trained specialist, patient-inconvenient, might require contrast agents, costly
Scintigraphy, PET, SPECT [112,125-133]	Imaging thyroid, parathyroid, pituitary, adrenal, assessing diabetes mellitus (i.e. imaging pancreas, blood vessels, brain, heart and/or adipose tissue), endocrine tumours, reproductive glands	Whole-body imaging, high resolution-to-depth ratio, high contrast, functional information, molecular contrast	Ionizing radiation, not real-time, contrast agents, long scanning times, not portable, difficult to use, inconvenient for patient

Table 2: Optoacoustic contrast

Term[a]	Name	Feature visualized
HbO_2	Oxygenated haemoglobin	Vasculature (arteries, arterioles) and oxygenated haemoglobin in tissue
Hb	Deoxygenated haemoglobin	Vasculature (veins, venules) and deoxygenated haemoglobin distribution in tissue
$Hb+HbO_2$	TBV	Vasculature (total), inflammation
Ratio of HbO_2 to TBV	SO_2	Tissue oxygenation and hypoxia, vascular oxygenation
Change in TBV over time	TBV rate	Tissue perfusion
Change in SO_2 over time	SO_2 rate	Oxidative metabolism
Lipids	Lipids	Adipose tissue, lipid concentration in vasculature or tissue
Water	Water	Distribution of water in tissue

[a]Physiological parameters that can be measured by optoacoustics based on endogenous light absorbers, such as haemoglobin, lipids and water. Hb, haemoglobin; TBV, total blood volume; SO_2, oxygen saturation.

Figure 1. Optoacoustic technology. a | Classification of optoacoustic technologies according to penetration depth and resolution. **b |** For each optoacoustic frame, a corresponding ultrasound frame is recorded. Finally, recorded MSOT data (multispectral stacks of images taken at different wavelengths (W_x) are spectrally unmixed into images showing the spatial distribution of chromophores, such as the oxygenated and deoxygenated haemoglobin, lipids and water. **c |** Light pulses (red arrow) of different near-infrared wavelengths illuminate tissue. The ultrasound waves (blue arrow) produced after the absorption of each light pulse are reconstructed into an optoacoustic frame. OAM, optoacoustic microscopy, RSOM: raster-scan optoacoustic mesoscopy, MSOT: multispectral optoacoustic tomography.

Figure 2. Clinical optoacoustics in endocrinology: thyroid and microvascular imaging. A | A hand-held optoacoustic unit. Light is shown by a red arrow and ultrasound by a blue arrow. The device comprises an: ultrasound unit, optoacoustic unit and a computer. **B |** Multispectral optoacoustic tomography (MSOT) imaging of the thyroid in healthy volunteers and patients. (Ba) Ultrasound imaging of the neck in a healthy volunteer. (Bb) Optoacoustic image of the total blood volume (TBV) for the ultrasound image of (Ba). (Bc) Optoacoustic thyroid TBV image of a healthy volunteer. (Bd) Optoacoustic thyroid TBV image of a patient with Graves disease. (Be) Ultrasound image of a thyroid nodule. N: nodule. (Bf) Optoacoustic oxygen saturation (SO_2) image weighted with the optoacoustic TBV signal (SO_2*TBV) corresponding to the ultrasound image of (Be). Scale bars: 1 cm. White dashed line: skin. Colour bars: min to max ultrasound or optoacoustic signal intensity. **C |** Skin microvascular imaging with Raster-scan optoacoustic mesoscopy (RSOM). (Ca) RSOM principle of operation. Motorized stages (M) move the optical fibres, which deliver light (green arrows), and the ultrasound transducer, which records the produced ultrasound (blue arrow). (Cb) RSOM image of skin vasculature. Colour bar represents the size of the imaged microvessels: with red the large vessels, with orange the middle-sized and with green the small vessels. (Cc) RSOM image of skin microvasculature before hyperthermia. Inset: a small vessel with a diameter of 19.3 um. (Cd) RSOM image after hyperthermia. Inset: same small vessel as in (Cc) with an increased diameter of 30.3 um. Scale bars: 0.5 mm. C, common carotid artery; DR, dermis; EP, epidermis; M, muscle; T, thyroid. Figure 2 part B: this research was originally published in JNM[79]. W. Roll et al. Multispectral optoacoustic tomography of benign and malignant thyroid disorders - a pilot study. *J Nucl Med*

2019;60:1461-1466 © SNMMI. Figure 2 part Cb is adapted from ref [46], Springer Nature Limited. Figure 2 part Cc and part Cd are adapted from ref [69], CC BY 4.0 (http://creativecommons.org/licences/by/4.0/).

Figure 3. Clinical optoacoustics in endocrinology: imaging metabolism. A | Near-infrared absorption spectra of oxygenated haemoglobin, deoxygenated haemoglobin, lipids and water. **B |** Imaging metabolism with multispectral optoacoustic tomography (MSOT). (Ba) PET–MRI of the brown adipose tissue (BAT) of a volunteer. (Bb) Boxplots of the normalized optoacoustic signals within the BAT, muscle and skin before and after cold exposure (*n* = 3 volunteers). (Bc) MRI in the plane marked in (Ba) with yellow dashed line. Scale bar: 5 cm. (Bd) MRI of the supraclavicular region marked with a yellow-dashed-line box in (Bc). Scale bar: 5 mm. Colour bar ranges from min to max MRI signal. (Be) PET–MRI of the same region showing 18F-fluorodeoxyglucose uptake within the BAT region (colour bar). Scale bar: 5 mm. (Bf) MSOT image of the same region. Colour bar ranges from min to max MSOT signal. Scale bar: 1 mm. Top arrow: BAT. Bottom arrow: muscle. (Bg) BAT MSOT image before cold exposure corresponding to the region indicated by the top arrow in (Bf). (Bh) Same region as in (Bg) showing BAT after cold exposure. The arrows show an increase in optoacoustic signal before and after BAT activation. (Bi) MSOT image of muscle before cold exposure corresponding to the region indicated by the bottom arrow in (Bf). (Bj) Same region as in (Bi) showing muscle after cold exposure. Colour bar ranges from min to max MSOT signal. Figure 3 is adapted with permission from ref [21], Elsevier.

Figure 4. Preclinical optoacoustics in endocrinology: imaging BAT. A | Small-animal imaging with optoacoustics. Light is shown by a red arrow and ultrasound by the blue arrow. The imaging station comprises an ultrasound unit, optoacoustic unit, anaesthesia unit, computer and a temperature controller (TC). **B |** Multispectral optoacoustic tomography (MSOT) of interscapular brown adipose tissue (iBAT) in mouse. (Ba) Anatomical optoacoustic image at 800 nm. (Bb) Cryo-section of same region. (Bc) Optoacoustic image of oxygenated haemoglobin. (Bd) Close-up view of iBAT-oxygenated haemoglobin before (-NE) and after (+NE) the injection of noradrenaline. (Be) Optoacoustic image of deoxygenated haemoglobin. (Bf) Close-up view of iBAT-deoxygenated haemoglobin before (-NE) and after (+NE) noradrenaline injection. Scale bars for (Ba), (Bc) and (Be): 4 mm. Scale bars for (Bd) and (Bf): 1 mm. (Bg) Boxplot of normalized optoacoustic signal for iBAT-oxygenated haemoglobin and deoxygenated haemoglobin before (-NE) and after (+NE) noradrenaline injection. **P* <0.01. (Bh) Normalized optoacoustic signal for oxygenated haemoglobin along the profile of (Ba) before (-NE) and after (+NE) noradrenaline injection. (Bi) Normalized optoacoustic signal for deoxygenated haemoglobin along the profile of (Ba) before (-NE) and after (+NE) noradrenaline injection. Colour bar: minimum to maximum optoacoustic signal. SV, Sulzer's vein. Figure 4 part B is adapted with permission from ref [21], Elsevier and from ref [134], Springer Nature Limited.

Figure 5. Imaging of cellular metabolites using mid-infrared optoacoustic microscopy. a | Bright-field image of 3T3-L1 cells that have been differentiated into adipocyte cells. **b |** Label-free mid-infrared optoacoustic microscopy (MiROM) image at 2,857 cm^{-1} wavelength (CH_2 vibration: corresponding to the excitation of stretching vibrations of carbon–hydrogen bonds composing the aliphatic tails of lipids) showing endogenous lipid contrast and corresponding to the image of a single adipocyte (dashed-line box). **c |** Label-free MiROM image at 1,550 cm^{-1} wavelength (amide II) showing protein contrast over the same region. **d |** Overlay of lipid and protein maps over the same region. Colour bars range from min to max of the optoacoustic signal at the corresponding wavelength. Common scale bars: 10 µm. **e–g |** Monitoring isoproterenol-induced lipolysis in 3T3-L1 adipocytes using MiROM imaging at 2,857 cm^{-1} through time (part e corresponds to minute 86, f to minute 172 and g to minute 257). Green and red dashed-line circles: two individual adipocytes. White arrow: follows the remodelling of a single lipid droplet after the addition of isoproterenol (ISO). Common colour bars range from the minimum to the maximum of the measured optoacoustic signal. Common scale bars: 40 µm. **h |** Change of relative lipid contrast over time within the two circle-marked individual adipocytes of images e to g. The time point of isoproterenol addition is indicated with

the red arrow (~minute 100). ROI, region of interest. VIS, visible light. Figure 5 is adapted from ref [34], Springer Nature Limited.

Glossary

Multi-spectral optoacoustic tomography

Macroscopic imaging technology that generates real-time images of tissues in clinical and preclinical applications.

Raster-scan optoacoustic mesoscopy

Mesoscopic imaging technology that produces volumetric images of tissues and is mainly used for skin and microvascular applications.

Mid-infrared optoacoustic microscopy

Label-free microscopic technology that provides endogenous biomolecular contrast images of cellular metabolites and their dynamics.

Chromophores

These are the parts of a molecule that absorb light at a particular frequency, to give a molecule its specific colour.

Tyrosinase

An enzyme that facilitates the production of the pigment eumelanin and can be permanently expressed in engineered cells to provide strong optoacoustic contrast.

Optoacoustic imaging enables the non-invasive and label-free imaging of the structure and function of organs, tissues and cells. This Review highlights key progress with optoacoustic imaging technology for applications in endocrinology and metabolism, with a specific focus on multispectral optoacoustic tomography and raster-scan optoacoustic mesoscopy.

Figure 1

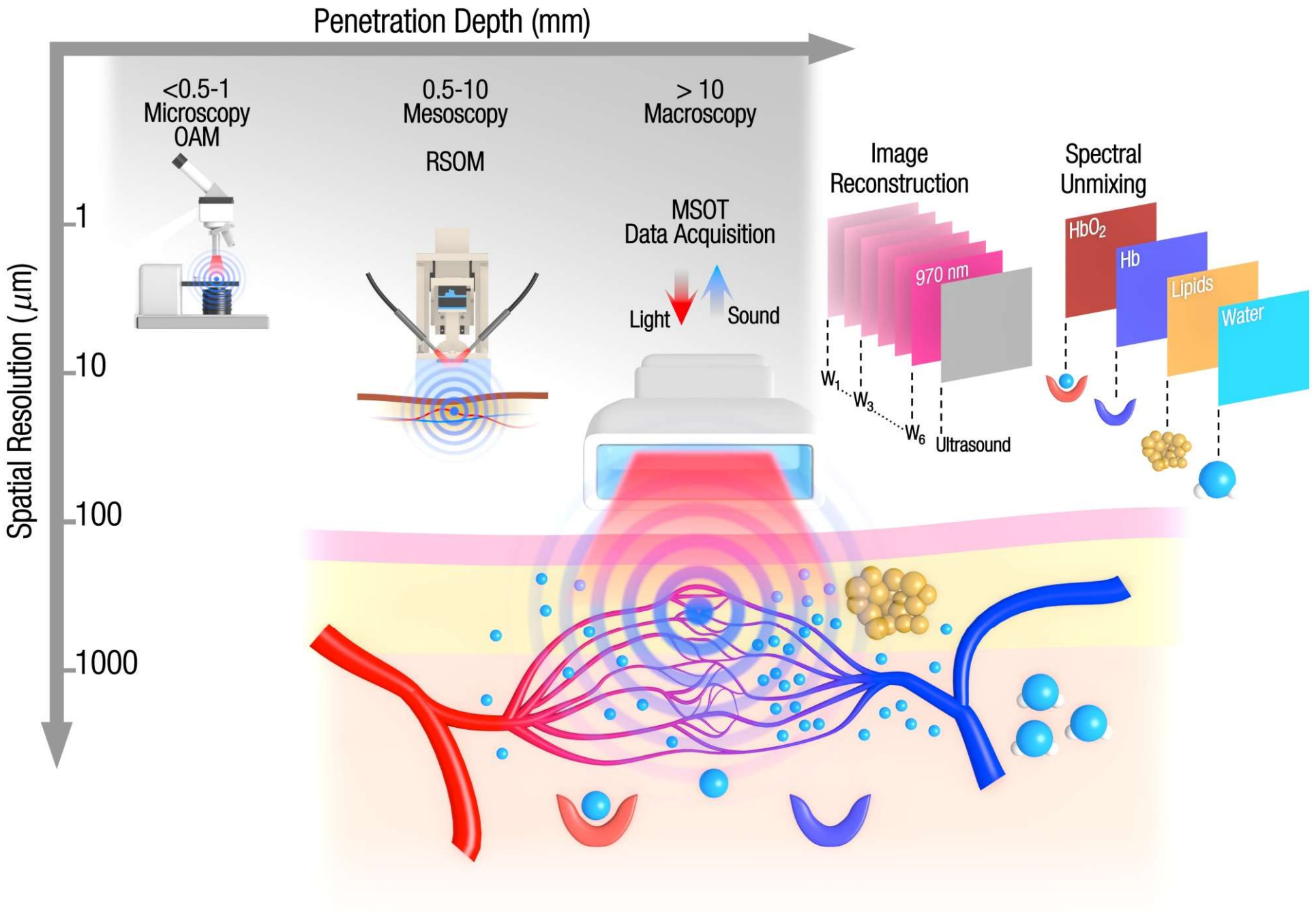
Penetration Depth (mm)
<0.5-1
Microscopy
OAM
0.5-10
Mesoscopy
RSOM
> 10
Macroscopy
MSOT
Data Acquisition
Light
Sound
Image
Reconstruction
970 nm
W1
W3
W6
Ultrasound
Spectral
Unmixing
HbO2
Hb
Lipids
Water
Spatial Resolution (μm)
1
10
100
1000

Figure 2

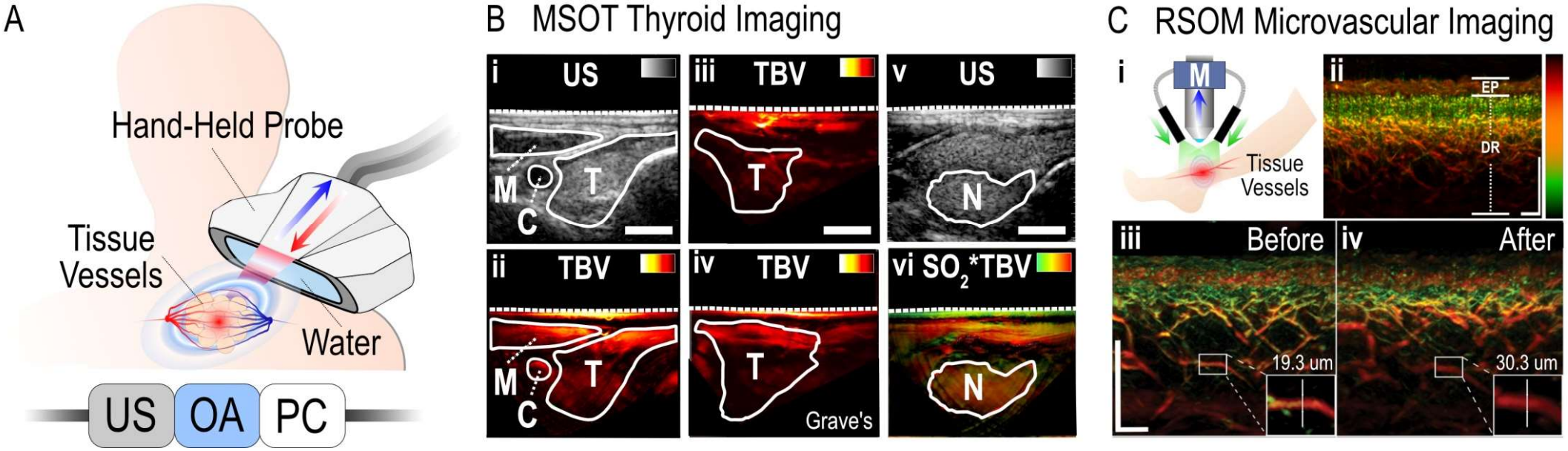
A
Hand-Held Probe
Tissue
Vessels
Water
US
OA
PC
B MSOT Thyroid Imaging
i US
iii TBV
v US
ii TBV
iv TBV
vi SO2*TBV
M
C
T
N
Grave's
C RSOM Microvascular Imaging
i
M
Tissue
Vessels
ii
EP
DR
iii Before
iv After
19.3 um
30.3 um

Figure 3

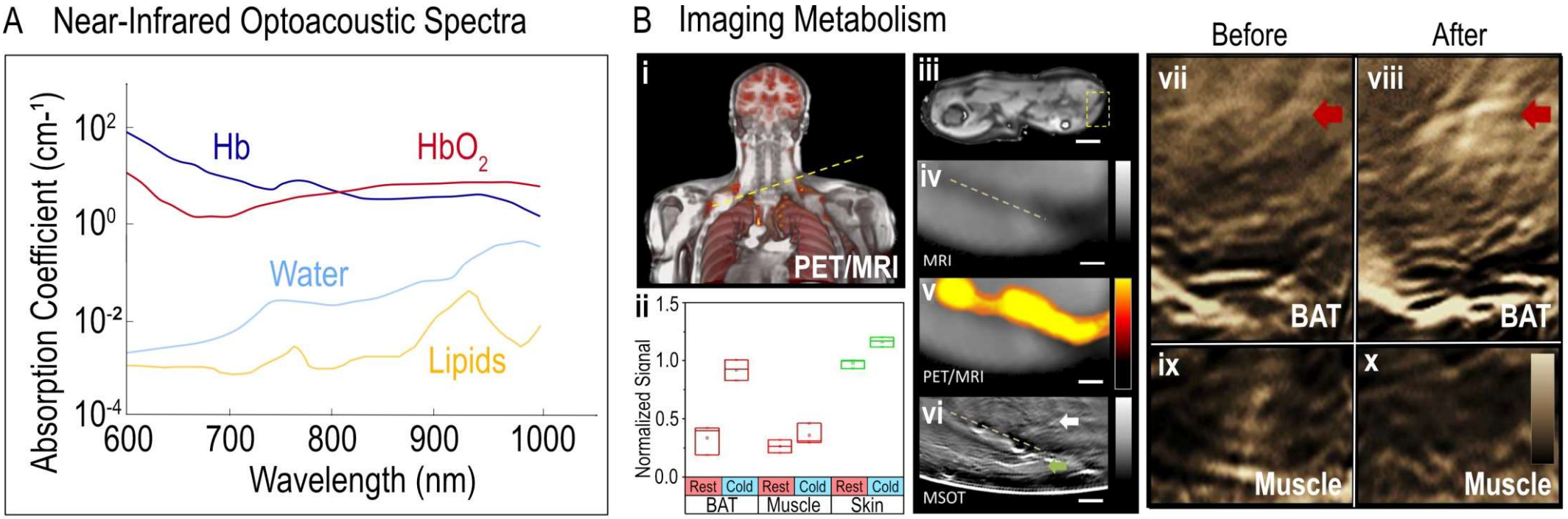
A Near-Infrared Optoacoustic Spectra
Absorption Coefficient (cm-1)
10^2
10^0
10^-2
10^-4
Hb
HbO2
Water
Lipids
600
700
800
900
1000
Wavelength (nm)
B Imaging Metabolism
i
PET/MRI
ii
Normalized Signal
1.5
1.0
0.5
0.0
Rest
Cold
Rest
Cold
Rest
Cold
BAT
Muscle
Skin
iii
iv
MRI
v
PET/MRI
vi
MSOT
Before
After
vii
BAT
viii
BAT
ix
Muscle
x
Muscle

Figure 4

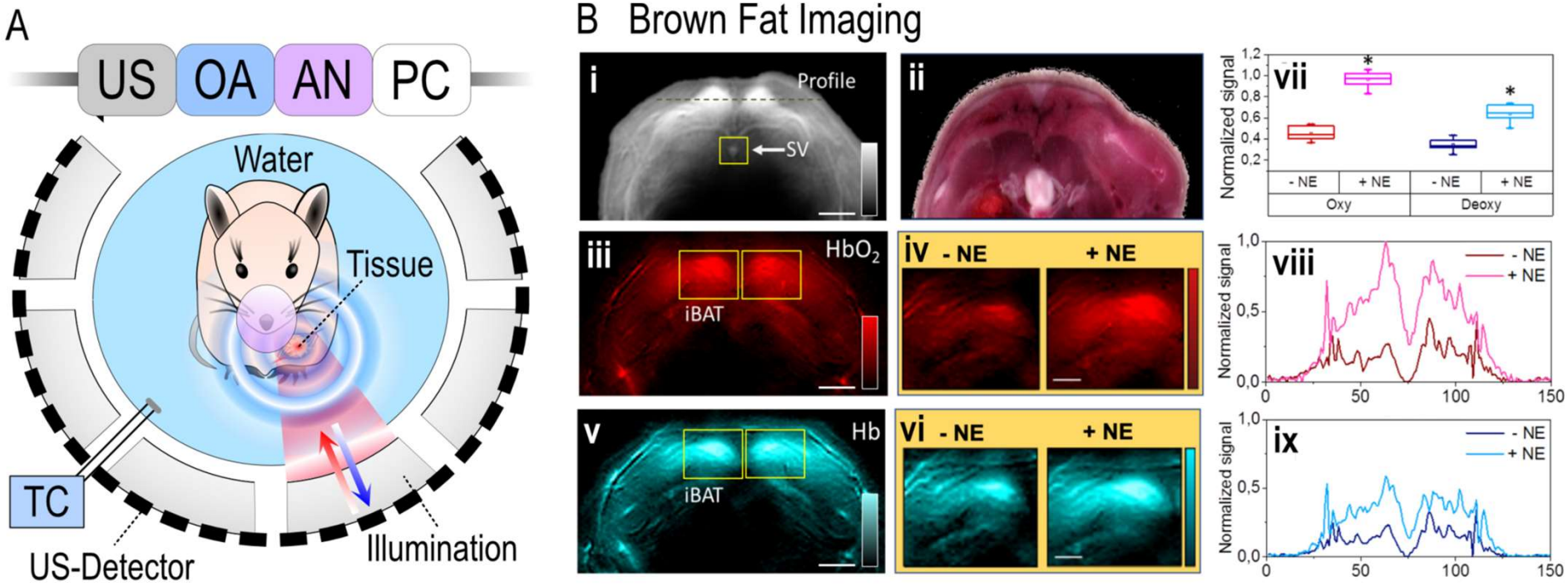
A
US
OA
AN
PC
Water
Tissue
TC
US-Detector
Illumination
B Brown Fat Imaging
i
Profile
SV
ii
iii
HbO2
iBAT
iv - NE
+ NE
v
Hb
iBAT
vi - NE
+ NE
vii
Normalized signal
- NE
+ NE
- NE
+ NE
Oxy
Deoxy
viii
Normalized signal
- NE
+ NE
ix
Normalized signal
- NE
+ NE

Figure 5

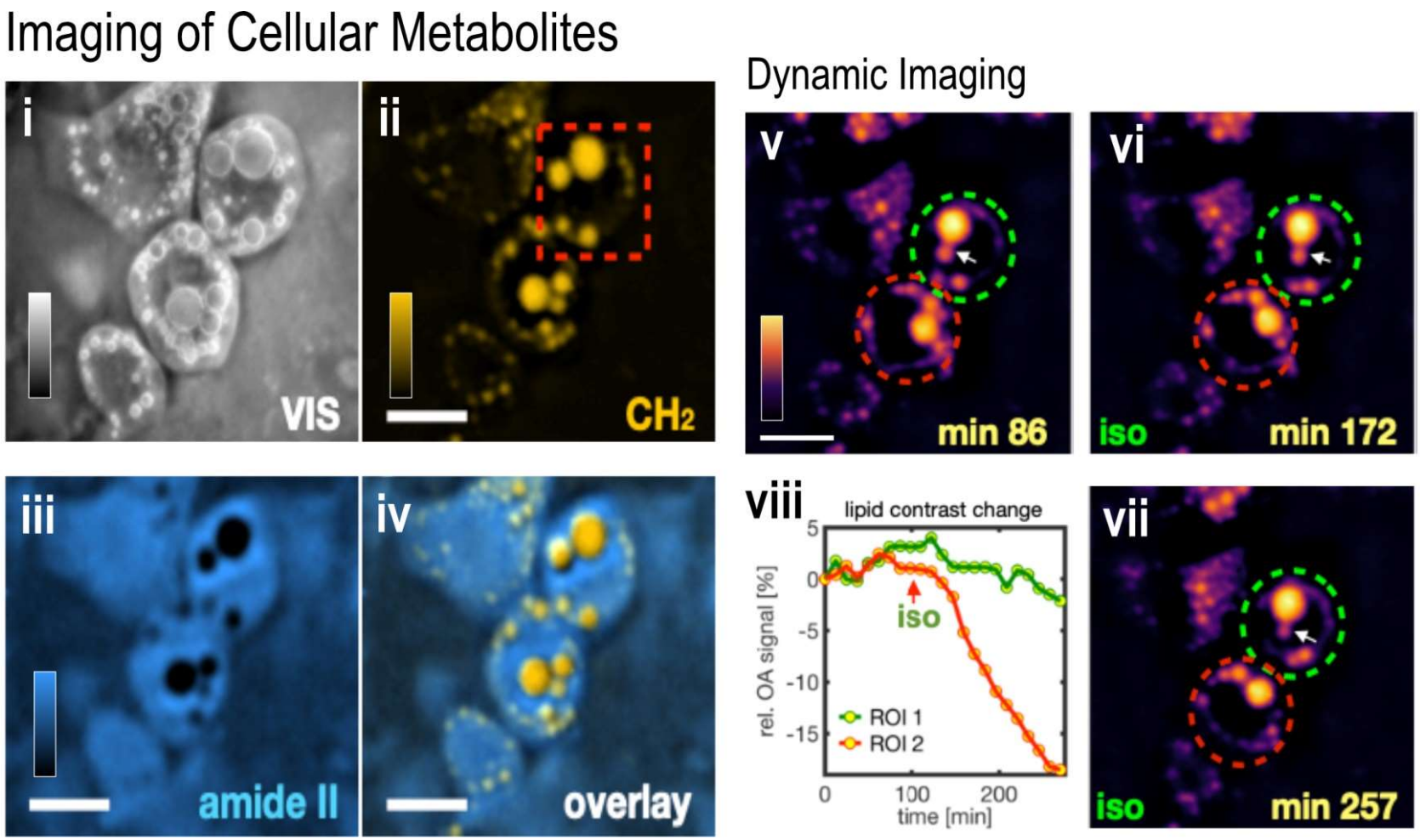
Imaging of Cellular Metabolites
i
VIS
ii
CH2
iii
amide II
iv
overlay
Dynamic Imaging
v
min 86
vi
iso
min 172
viii
lipid contrast change
rel. OA signal [%]
5
0
-5
-10
-15
iso
ROI 1
ROI 2
0
100
200
time [min]
vii
iso
min 257